

Research Paper

Nano-drug System Based on Hierarchical Drug Release for Deep Localized/Systematic Cascade Tumor Therapy Stimulating Antitumor Immune Responses

Yuchu He^{1,2}, Cong Cong¹, Xiaoling Li¹, Ruiyan Zhu^{1,3}, Anshuo Li⁴, Shuxian Zhao¹, Xiaowei Li¹, Xin Cheng¹, Mengxue Yang¹, Dawei Gao^{1,2}✉

1. Applied Chemistry Key Laboratory of Hebei Province, Department of Bioengineering, Yanshan University, No.438 Hebei Street, Qinhuangdao, 066004, China.
2. State Key Laboratory of Metastable Materials Science and Technology, Yanshan University, Qinhuangdao 066004, P. R. China.
3. Hebei Province Asparagus Industry Technology Research Institute, Qinhuangdao, 066004, China.
4. Department of Prosthodontics Ninth People's Hospital Shanghai Jiao Tong University School of Medicine, 639 Zhizaoju Road, Shanghai 200011, China.

✉ Corresponding author: Prof. Dawei Gao, Tel: (+86)13930338376 E-mail: dwgao@ysu.edu.cn

© Ivyspring International Publisher. This is an open access article distributed under the terms of the Creative Commons Attribution (CC BY-NC) license (<https://creativecommons.org/licenses/by-nc/4.0/>). See <http://ivyspring.com/terms> for full terms and conditions.

Received: 2019.01.26; Accepted: 2019.03.27; Published: 2019.05.04

Abstract

Inaccessibility of deep-seated malignant cells in the central region of tumors and uncontrollable tumor recurrence represent a significant challenge for conventional synergistic cancer therapy. Herein, we designed a novel nanoplatform based on hierarchical drug release for deep cascade cancer therapy including localized photothermal therapy, systematic chemotherapy, and elicited immune responses.

Methods: The first-step chemotherapy could be carried out by polydopamine (PDA) releasing doxorubicin (DOX) in the specific microenvironment of lysosomes (pH 5.5). The branched gold nanoshells and PDA converted the light to heat efficiently to accomplish the second-step photothermal therapy and collapsed biomimetic vesicles (BVs) to release paclitaxel (PTX), which promoted the third-step of chemotherapy and triggered immune responses.

Results: After 10 days of treatment, there were no obvious residual tumors in tumor-bearing mice. Significantly, 10 days after stopping treatment, mice in the drug immune-therapeutic group showed little tumor recurrence (1.5 times) compared to substantial recurrence (20 times) in the conventional treatment group.

Conclusion: The hierarchical drug release and cascade therapeutic modality enhance the penetration of drugs deep into the tumor tissue and effectively inhibit recurrence. This cascade therapeutic modality provides a novel approach for more effective cancer therapy.

Key words: Hierarchical drug release; Tumor recurrence; Biomimetic vesicles; Cascade cancer therapy; Immune responses

Introduction

Cancer, as one of the deadliest diseases, has resulted in growing mortality in recent decades [1]. Conventional cancer therapy such as chemotherapy [2] or radiotherapy [3] alone is not effective in eliminating the tumors. Therefore, synergistic therapy is commonly used for enhancing the efficacy of cancer treatment [4, 5]. Recently, versatile modalities of

synergistic therapy have shown success in treating several advanced cancers [6-8]. Nevertheless, there are still some formidable challenges for synergistic cancer therapy and its clinical efficacy. First, although the efficacy of synergistic therapy is significant, it is hard to suppress the tumor recurrence due to the existing residual tumor cells [9]. Second, the limitation

of synergistic therapy to eliminate the deep-seated tumor cells inevitably leads to tumor recurrence and metastasis [10]. And third, the localized hyperthermia and reactive oxygen species (ROS) damage to the normal tissues and immune system instigate negative interactions among different therapeutic modalities [11]. Given the limitations with synergistic therapy, it is urgently desirable to develop a novel therapeutic strategy for hierarchical drug release combining localized and systematic therapies, a deep penetration into the tumors, and nontoxicity to the immune system and normal tissues.

In the past several years, drug delivery systems based on nanotechnology have been actively explored for their efficiency in cancer diagnosis and treatment [12]. In this respect, the biomimetic vesicle (BVs)-based drug carriers have attracted much attention due to their biocompatibility, degradable soft template, controllable drug release *via* temperature-responsive phase transformation, and manageable size distribution [13]. These drug carriers could enhance the delivery of chemotherapeutic drugs such as paclitaxel (PTX), the first-line drug for efficient tumor eradication by inhibiting the disassembly of intracellular polymeric microtubules [14]. Furthermore, low dose PTX has been shown to be an immunologic adjuvant stimulating the immune system to eliminate residual tumors [15]. Thus, PTX has been widely applied in chemo and immunotherapy [16, 17].

Because of the differential thermal tolerance of tumor versus normal cells, photothermal therapy (PTT) as a noninvasive therapeutic modality leads to DNA damage and protein denaturation in tumors [18]. Furthermore, the combination of photothermal agents and drug carriers can promote controllable drug release and delivery. In this respect, due to their optical property of surface plasmon resonance (SPR) [19-22], gold nanomaterials have stimulated efforts in photothermal tumor therapy [23]. Given the deep tissue penetration of the near-infrared (NIR) laser resulting in minimal damage to the surrounding tissues [24], gold nanomaterials, which can achieve the redshift of SPR peak to the NIR region, have been designed and extensively applied in localized and precise photothermal therapy. However, low concentration of gold needs stronger exposure of laser, which poses the potential risk of damaging the surrounding tissues. The high concentration of gold nanomaterials needed for therapeutic efficacy, on the other hand, is a serious drawback because of the toxicity to normal tissues [25]. To address these issues, polydopamine (PDA), which has excellent biocompatibility and adhesion, was used to coat the gold nanomaterials to augment their biosafety [26].

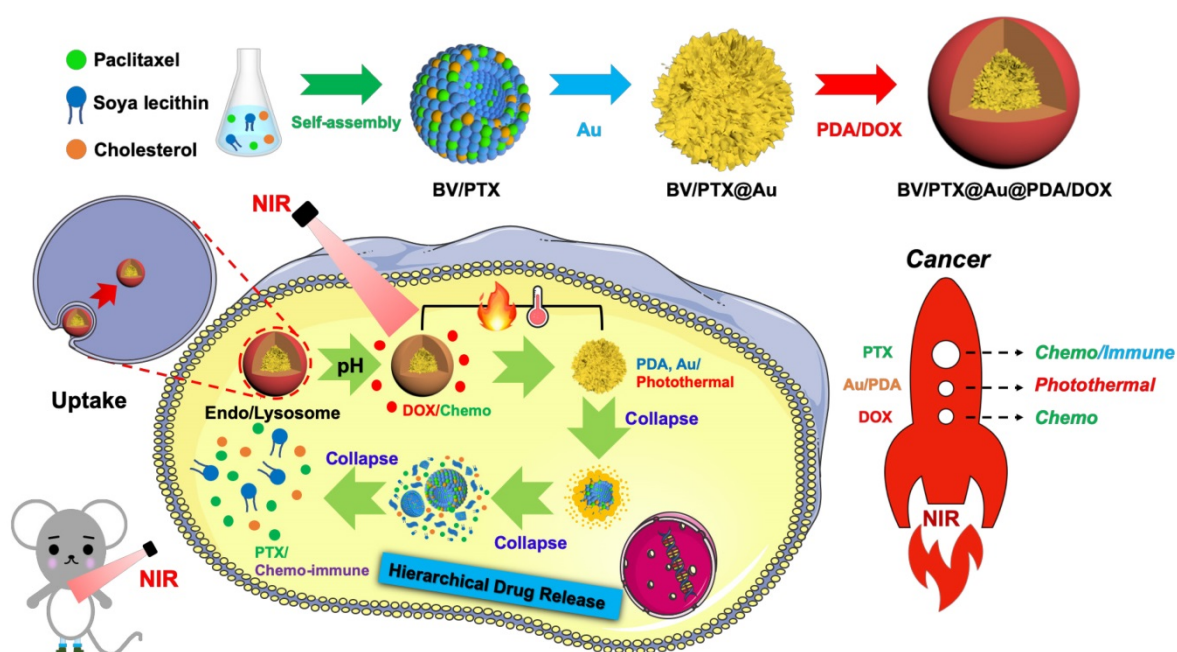
Furthermore, inspired by its stimuli-responsive drug release in hyperthermal or acidic condition [27], PDA was capitalized as a responsive drug carrier [28]. Also, since PDA is absorptive in the NIR region, it is considered to be a potential PTT agent as well [29]. Thus, we utilized the advantages of PDA to reduce the cytotoxicity of high concentration of gold and photodamage of the high-power laser.

Herein, we designed an emerging nanoplatform based on hierarchical drug release for deep localized (PTT) and systematic (chemo and immune responses) cascade cancer therapy. During the water-oil self-assembly, PTX biomimetic vesicles (BV/PTX) were formed and modified by branched gold nanoshells (BV/PTX@Au) *via* seeded growth. Thereafter, the BV/PTX@Au were coated with doxorubicin (DOX)-loaded PDA to form the final drug delivery system (BV/PTX@Au@PDA/DOX). Because of the acidic environment of the lysosomes, when the BV/PTX@Au@PDA/DOX reached the tumor cells, PDA released the DOX in the first-step chemotherapy. Subsequently, under the 808 nm laser irradiation, the branched gold nanoshells and PDA converted the light to heat to achieve second-step photothermal therapy. Finally, with the rising temperature, the branched gold nanoshells and biomimetic vesicles collapsed and released the PTX to complete the third-step of chemotherapy and immune responses (**Scheme 1**). The BV/PTX@Au@PDA/DOX could drastically destroy the residual tumor cells and efficiently prevent localized tumor recurrence. We further studied the underlying mechanism of the immune responses triggered by PTX. We believe that our work provides a promising therapeutic strategy, which is different from conventional synergistic therapy and represents a significant development in the field of oncology.

Methods

Synthesis of BV/PTX@Au@PDA/DOX

Paclitaxel, soya lecithin, and cholesterol were added into ethanol solution. Polyethylene glycol-2000 was solubilized in phosphate buffered saline (PBS). Subsequently, the lipid phase was mixed with the water phase to form BV/PTX. Glutathione (GSH) (0.5 mg/mL) was then added to BV/PTX and stirred for 4 hours. Subsequently, BV/PTX@AuNPs were synthesized by adding Au seeds to the prepared BV/PTX. Finally, AuCl₃ (2 mM) and NH₂OH·HCl (100 mM) were mixed into the BV/PTX@AuNPs solution. After stirring for 6 h, 300 μL of 4 mM AuCl₃ and 50 μL of NH₂OH·HCl (150 mM) were added to prepare the BV/PTX@Au. PDA was prepared by stirring 0.5 mg mL⁻¹ dopamine (DA) in Tri-HCl buffer



Scheme 1. Schematic diagram of the synthetic route of BV/PTX@Au@PDA/DOX nanoparticle (top) and the hierarchical drug release process (bottom) of pH-activated and NIR-triggered localized/systematic cascade cancer therapy in tumor-bearing mice.

(pH 7.4) for 2 h, centrifuging and collecting the supernatant. Subsequently, 0.1 mg mL^{-1} DOX was added dropwise into the PDA solution to obtain the DOX-loaded PDA (PDA/DOX). Finally, the PDA/DOX was added to the BV/PTX@Au solution and incubated for 6 h to obtain BV/PTX@Au@PDA/DOX, which was stored at 4°C for further characterization.

Drug release and photothermal effect

The DOX release under different pH values and PTX release from BV/PTX@Au@PDA/DOX with irradiation were investigated using the dialysis method. At 2nd and 4th h, the solutions were irradiated by 808 nm laser (1.5 W/cm^2 , 5 min).

To evaluate the photothermal performance of the prepared samples 0.5 mL of BV/PTX@Au@PDA/DOX and control samples (BV/PTX, BV/PTX@AuNPs and BV/PTX@Au) were exposed to 808 nm laser, and the temperature of the solutions was measured every 30 s. The photothermal conversion efficiency (η) [30] of BV/PTX@Au@PDA/DOX was calculated by:

$$\eta = \frac{h\Delta T_{\max} - Q_s}{I(1 - 10^{-A_\lambda})} \quad (1)$$

Where η was the conversion efficiency from an 808 nm laser energy to thermal energy, h was the heat transfer coefficient of BV/PTX@Au@PDA/DOX, A was the area cross section of irradiation, T_{\max} was the steady-state maximum temperature change, Q_s was the heat associated with the light absorbance of the solvent measured using solvent without

Au@PDA/DOX, I was the incident laser power, and A_λ was the absorbance of BV/PTX@Au@PDA/DOX at 808 nm. In this equation, the value of hA was unknown for calculation. To get hA , the variable θ was introduced:

$$\theta = \frac{T - T_{\text{amb}}}{\Delta T_{\max}} \quad (2)$$

Where T was the solution temperature, T_{amb} was the ambient room temperature. The value of hA could be derived from the following:

$$hA = \frac{mc_p}{\tau} \quad (3)$$

Where m and c_p were the mass and heat capacity of water, respectively. During the cooling process, the thermal time constant τ could be calculated as follows:

$$t = -\tau \ln \theta \quad (4)$$

The photothermal conversion efficiency could be calculated when the thermal time constant τ was obtained.

Cellular uptake and cytotoxicity in vitro

The antitumor effect of all formulations *in vitro* was studied by HeLa cells using the MTT assay. The cells were cultured in Dulbecco's Modified Eagle's Medium (DMEM) containing 10% fetal bovine serum and 1% penicillin/streptomycin at 37°C containing 5% CO_2 . HeLa cells were cultured in a 6-well plate for 24 hours, BV/Cour6@Au@PDA/DOX was added to the plate with DOX concentration of $10 \mu\text{g/mL}$. The cells were then washed with cold PBS three times and fixed with 4% paraformaldehyde for 10 min. Finally,

the cells were observed under an inverted fluorescence microscope. Hela cells were also seeded in 96-well plates at a density of 5.0×10^4 cells per well and cultured for 24 hours. The cells were incubated with fresh cell medium containing prepared nanomedicine with different concentrations of PTX (2.5 to 20 $\mu\text{g}/\text{mL}$) and DOX (1.25 to 10 $\mu\text{g}/\text{mL}$) for 24 hours. For the study of tumor inhibition, the BV@Au@PDA/DOX and BV/PTX@Au@PDA/DOX were laser irradiated and then removed from the 96-well plates and fresh culture medium was added for continuous proliferation. The cell viability was analyzed by the MTT assay at 12, 24, 36, and 48 hours.

Cascade tumor therapy and biodistribution study *in vivo*

Kunming mice were inoculated subcutaneously with the mouse cervical cancer cells U14 in the right armpit. U14 cells were purchased from the Chinese Academy of Medical Sciences Tumor Cell Bank (Beijing, China). The mice were injected with 200 μL of the following formulations by tail intravenous: 1: Saline, 2: BV/PTX, 3: BV/PTX@Au, 4: BV/PTX@Au with laser irradiation, 5: BV@Au@PDA/DOX, 6: BV@Au@PDA/DOX with laser irradiation, 7: BV/PTX@Au@PDA/DOX, and 8: BV/PTX@Au@PDA/DOX with laser irradiation. The injected Au concentration in the mouse (group 3 to 8) was 44 $\mu\text{g}/\text{mL}$. During the cascade therapy, the tumor sizes and body weights were measured every other day. Tumor volumes (V) were measured as [31]:

$$V = (\text{tumor length}) \times \frac{(\text{tumor width})^2}{2} \quad (5)$$

Relative tumor volume was computed as:

$$\text{RTV} = V/V_0 \quad (V_0 \text{ means initial tumor volume}) \quad (6)$$

After different time points (8 hours, 24 hours and 10 days), the animals were sacrificed and the major organs (heart, liver, spleen, lung, and kidney) and tumors were removed, washed, weighed, and freeze-dried. The tissue debris was removed by centrifugation at 8000 rpm for 10 min. After dilution, the Au contents were measured by ICP-MS.

Biosafety study and histology analysis *in vivo*

The relative liver and kidney functional factors were tested using sera of the mice by enzyme-linked immune sorbent assay (ELISA), including alanine aminotransferase (ALT), aspartate aminotransferase (AST), blood urea nitrogen (BUN), alkaline phosphatase (ALP), albumin (ALB) and total protein (TP). The tumor and the main organs of mice were examined by histological analysis (H&E staining). To study the tumor recurrence after treatment, two groups of 12 mice treated with BV@Au@PDA/DOX

or BV/PTX@Au@PDA/DOX with laser irradiation were observed sequentially during 10 days of non-treatment status.

Antitumor immune responses

After the mice were sacrificed, the relative immune factors (CD4, CD8, TNF- α and IL-6) were determined by ELISA using the sera of the mice treated with saline, BV@Au@PDA/DOX plus laser, and BV/PTX@Au@PDA/DOX plus laser. The levels of T memory cells (CD44) were assessed by ELISA using the ocular blood of mice treated with BV@Au@PDA/DOX under the laser and BV/PTX@Au@PDA/DOX under the laser. The numbers of CD4 and CD8 T cells in tumor cell suspensions were also analyzed using CD4-PE and CD8-APC antibodies by flow cytometry.

Results and Discussion

Synthesis and characterization

The PTX-loaded biomimetic vesicles (BV/PTX) were synthesized by water-oil self-assembly using phospholipid, cholesterol, and PBS. Modification of branched gold nanoshells (BV/PTX@Au) was realized by the seeded growth method, and the BV/PTX@Au was coated with DOX-loaded PDA to form BV/PTX@Au@PDA/DOX. TEM images of the synthetic process of BV/PTX@Au@PDA/DOX are shown in **Figure 1A** indicating the hierarchical assembly process of branched gold nanoshells and PDA. Gold nanoparticles combined with the BV/PTX via the Au-S bond and grew continuously to shape the gold nanoshells. The discrepancy of crystal lattice energy on the surface of gold nanoshells during the process of gold growth led to the formulation of branched gold nanoshells. The structure had a better photothermal effect compared with plain gold nanoshells. Subsequently, DOX-loaded PDA was firmly adhered on the surface of BV/PTX@Au. Energy Dispersive Spectrometer (EDS) analysis (**Figure 1B**) was applied to investigate the component elements of the BV/PTX@Au@PDA/DOX which indicated the successful modification of branched gold nanoshells (element Au) and DOX-loaded PDA (element O). UV-vis spectra exhibited that BV/PTX@Au@PDA/DOX was highly absorptive in the NIR window (650 ~ 900 nm) resulting in the excellent photothermal conversion effect. Furthermore, the characteristic absorption peak of 490 nm of BV/PTX@Au@PDA/DOX showed the successful loading of DOX (**Figure 1C**). The photographs of formulations in UV-vis spectra are presented in Figure S1. According to the XRD analysis (Figure S2), the diffraction peak positions of BV/PTX@Au could be attributed to (111), (220), (200),

(222) and (311) planes of Au. It provided further evidence that the BV/PTX had been coated by branched gold nanoshells and their thickness calculated according to the Debye-Scherrer formula [32] was approximately 13 nm. The conjugation of the synthetic products was confirmed using the FTIR spectra and is shown in Figure S3. The staple properties of GSH were stretching vibration of N-H at 3351 cm^{-1} and 3253 cm^{-1} . The typical peak of the GSH at 2526 cm^{-1} was from the thiol groups (-SH). However, the characteristic peak of -SH vanished entirely in the spectra of the BV/PTX@Au and BV/PTX@Au@PDA/DOX which was caused by the form of an Au-S bond between branched gold nanoshells and -SH. The results indicated that

branched gold nanoshells coated on the surface of BV/PTX. **Figures 1D & E** display the size distribution and zeta potentials of BV/PTX@Au@PDA/DOX, respectively. The average size of BV/PTX and the BV/PTX@Au@PDA/DOX were $130.5 \pm 2.5\text{ nm}$ and $158.2 \pm 3.6\text{ nm}$ (PDI=0.214), respectively (PDI=0.198, Figure S4). Zeta potential of BV/PTX@Au@PDA/DOX was $-18.5 \pm 2.3\text{ mV}$, which indicated better stability in the body compared with electropositive nanocarriers. Additionally, the loading efficiencies of PTX and DOX in the BV/PTX@Au@PDA/DOX were about 90.6% and 13.7%, respectively, which were measured by UV-vis method. The coating efficiency of gold measured by ICP-MS was about 16.2%.

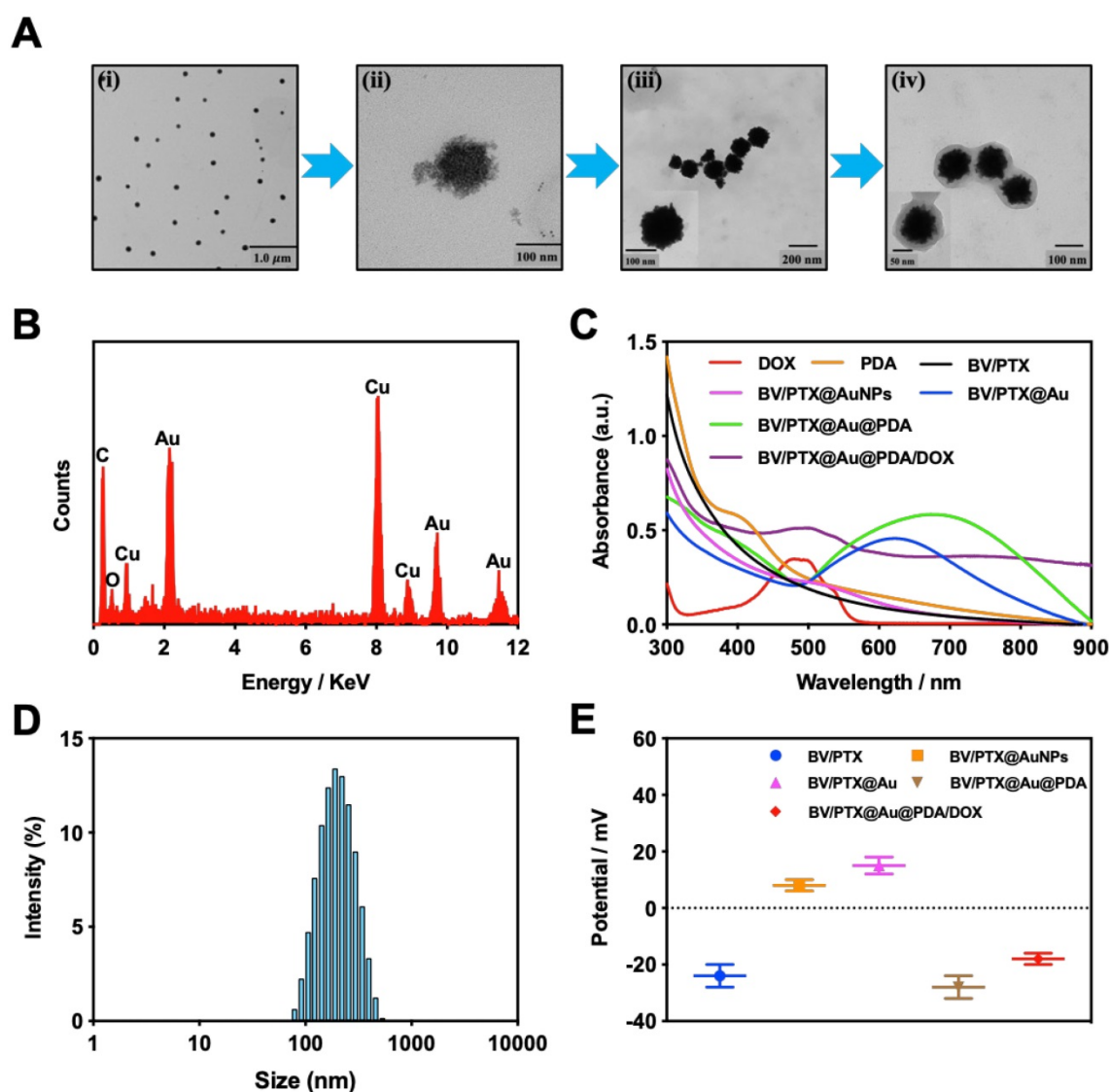


Figure 1. (A) TEM images of the products in the synthetic route: (i) BV/PTX, (ii) BV/PTX@AuNPs, (iii) BV/PTX@Au and (iv) BV/PTX@Au@PDA/DOX. (B) EDS of the BV/PTX@Au@PDA/DOX nanoparticles. (C) UV-vis absorption spectra of DOX, PDA, BV/PTX, BV/PTX@AuNPs, BV/PTX@Au, BV/PTX@Au@PDA and BV/PTX@Au@PDA/DOX. (D) Size distribution of BV/PTX@Au@PDA/DOX. (E) Zeta potentials of BV/PTX, BV/PTX@AuNPs, BV/PTX@Au, BV/PTX@Au@PDA and BV/PTX@Au@PDA/DOX.

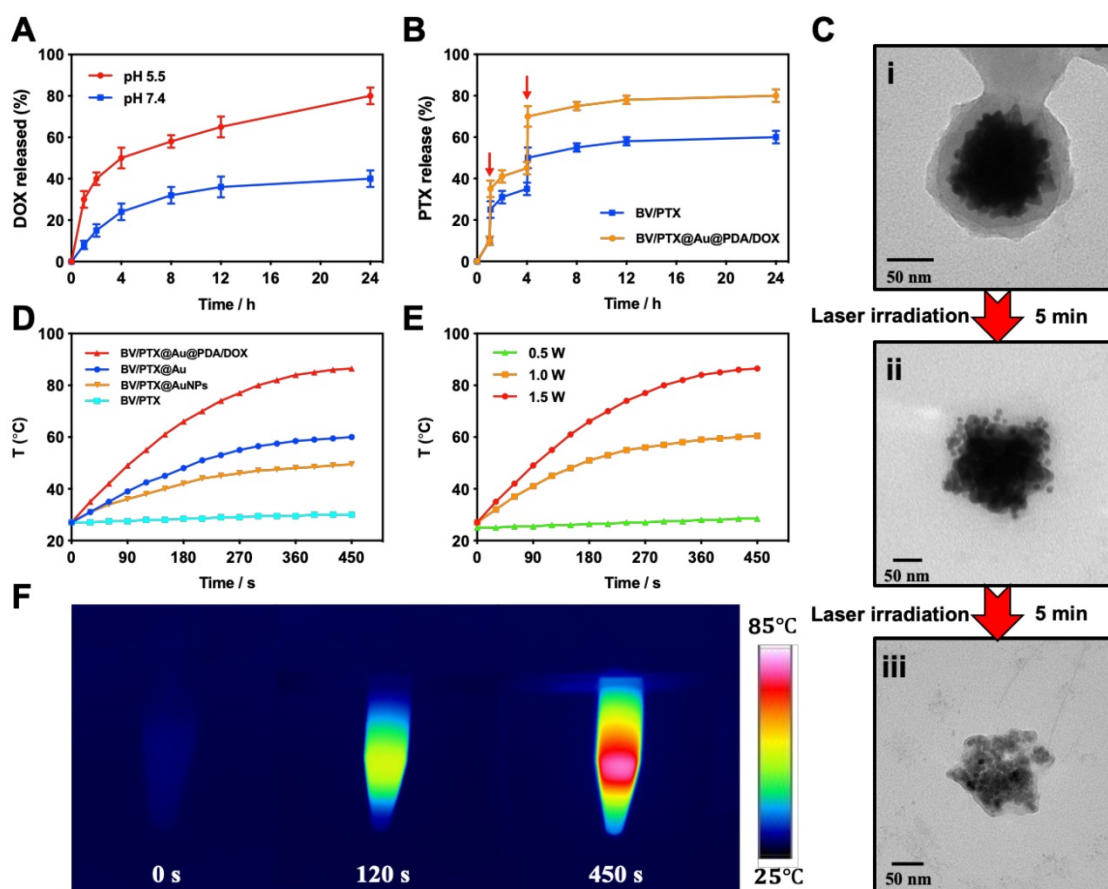


Figure 2. (A) DOX release from BV/PTX@Au@PDA/DOX at different pH (7.4 and 5.5) values as a function of cumulative time. (B) Accumulative PTX release from BV/PTX and BV/PTX@Au@PDA/DOX with laser irradiation for 5 min at the indicated time (Red arrows indicate the two points of laser irradiation). (C) TEM images of the collapse of BV/PTX@Au@PDA/DOX with (i) non-irradiation, (ii) irradiation once and (iii) irradiation twice. Data were expressed as mean \pm S.E. ($n = 3$). Temperature elevation profiles of (D) BV/PTX, BV/PTX@AuNPs, BV/PTX@Au and BV/PTX@Au@PDA/DOX under laser irradiation for 450 s and (E) BV/PTX@Au@PDA/DOX under laser irradiation with different power densities (0.5, 1.0 and 1.5 W cm⁻²). (F) Infrared thermal images of BV/PTX@Au@PDA/DOX in a tube with laser irradiation. Unless otherwise noted, an 808 nm laser was used at a power density of 1.5 W cm⁻².

Drug release

The release behavior of the anticancer drug, DOX, from BV/PTX@Au@PDA/DOX was studied under the imitated physiological environment of body fluids (PBS pH 7.4) and lysosomes (pH 5.5). The release amount of DOX was determined by UV-vis spectra. The drug release of BV/PTX@Au@PDA/DOX was pH dependent (Figure 2A), and DOX release was rapid at pH 5.5 with the accumulated release of $80.45 \pm 2.97\%$ in 24 hours. This rapid release could be due to the protonation and disintegration of PDA. In contrast, at pH 7.4, the release of DOX after 24 hours was less than $40.18 \pm 3.59\%$. We speculated that the minor release of DOX at pH 7.4 was caused by the excellent stability of PDA at neutral or alkaline conditions. The addition of 10% fetal bovine serum (FBS) did not affect the release of DOX and showed the potential performance of drug release *in vitro* (Figure S5). The PTX release in free PTX and BV/PTX@Au@PDA/DOX groups was also studied (Figure S6) which indicated the low leakage of PTX

from BV/PTX@Au@PDA/DOX without laser irradiation. After NIR laser irradiation to execute second-step photothermal therapy, the branched gold nanoshells and BVs collapsed and released PTX thus performing the third-step chemotherapy to induce the immune responses. The release of PTX was investigated by monitoring the PTX absorbance at 227 nm using UV-vis spectra. The BV/PTX@Au@PDA/DOX solution was irradiated twice under NIR laser for 5 min (1.5 W cm⁻²) at different irradiation time points indicating that PTX release was accelerated under laser irradiation (Figure 2B). After two cycles of laser irradiation (point in time: 1st and 4th hour), the release percentage of PTX reached $80.63 \pm 1.36\%$ after 24 hours which was much higher than that of BV/PTX ($61.43 \pm 2.12\%$) under the same condition. TEM images showed the collapsed process of the branched gold nanoshells and BV/PTX (Figure 2C). These data indicated the effective drug release of DOX at pH 5.5 and PTX under laser irradiation.

Photothermal performance

Inspired by the high absorption of BV/PTX@Au@PDA/DOX in the NIR region, we further studied the photothermal performance. As shown in **Figure 2D**, the temperature of BV/PTX@Au@PDA/DOX under 808 nm laser irradiation (1.5 W cm^{-2}) for 2 min could rapidly reach 55.0°C , and after 7.5 min increased to 86.5°C . Also, the temperature of BV/PTX@Au@PDA/DOX increased with the increase in power density from 0.5 to 1.5 W cm^{-2} (**Figure 2E**). Comparatively, a small temperature change ($\Delta T = 3.0^\circ\text{C}$) was observed for BV/PTX under the same conditions. We further studied the heating and cooling curves of the BV/PTX@Au@PDA/DOX (**Figure S7a, b**) to obtain the photothermal conversion efficiency of 43.6%, which was much higher than that of gold nanoshells-coated liposomes in our previous study (25.5%) [33]. The superior photothermal conversion efficiency of the BV/PTX@Au@PDA/DOX was attributed to the integration of branched gold nanoshells with PDA which was also visually displayed by the real-time infrared thermal imaging (**Figure 2F**).

Stability study

Stability is one of the significant factors for therapeutic effects, and the encapsulation efficiency is considered as the key criterion to evaluate colloidal stability [34]. In this study, the BV/PTX@Au@PDA/DOX was stored at 4°C for a period of 0, 5, 10, and 15 days. The reduced encapsulation efficiencies of PTX (**Figure S8a**) and DOX (**Figure S8b**) in BV/PTX@Au@PDA/DOX at 4°C were only 8% and 9%, respectively. These results directly validated the structural integrity and stability of BV/PTX@Au@PDA/DOX. Furthermore, the size distribution and zeta potential changes of the BV/PTX@Au@PDA/DOX were studied after 15 days of storage at 4°C as well. As shown in **Figure S8c**, the size distribution decreased from $158.2 \pm 2.3 \text{ nm}$ to $146.3 \pm 4.7 \text{ nm}$ and the zeta potential decreased from $-18.5 \pm 2.0 \text{ mV}$ to $-25.2 \pm 4.3 \text{ mV}$ (**Figure S8d**). We reasoned that the decrease of size distribution might be due to the falling off of PDA from the nanocarriers. Also, the continuous polymerization of the PDA in 15 days led to a decrease in zeta potential. The TEM images showing the morphologies of BV/PTX@Au@PDA/DOX before (**Figure S8e**) and after storage at 4°C for 15 days are displayed in **Figure S8f**. Overall, the results suggested that BV/PTX@Au@PDA/DOX exhibited good stability for a long time.

Cellular uptake and cytotoxicity *in vitro*

To investigate the cellular uptake of the

BV/PTX@Au@PDA/DOX, PTX was replaced by coumarin 6 (Cour6). Due to the fluorescence of Cour6 and DOX, the cellular uptake of inside BVs and outside PDA could be displayed precisely. HeLa cells were treated with BV/Cour6@Au@PDA/DOX for 24 hours, and flow cytometry was used to quantify the cellular uptake. The flow cytometry images of DOX (**Figure 3A**) and Cour6 (**Figure 3B**) of BV/Cour6@Au@PDA/DOX group were obtained compared to the control group. As shown in **Figure 3G**, the nuclei of HeLa cells were stained by Hoechst, and the DOX and Cour6 loaded on PDA and BVs, respectively, were present in the cytoplasm of HeLa cells indicating that the nanoparticles were taken up by the cells.

Following the uptake of BV/PTX@Au@PDA/DOX by HeLa cells for 24 hours, the cascade therapeutic effect *in vitro* was studied. Culture medium was removed, and the cells were washed by PBS for three times. Subsequently, the cells were irradiated with an 808 nm laser (1.5 W cm^{-2}). Cell viability was determined using the MTT assay. With the increase in the concentration of PTX and DOX, the cell viability decreased with or without laser irradiation; free drugs were used as controls (**Figure 3D, E**). The cytotoxicity of all the formulations (1: control, 2: BV/PTX, 3: BV/PTX@Au, 4: BV/PTX@Au with laser irradiation, 5: BV@Au@PDA/DOX, 6: BV@Au@PDA/DOX with laser irradiation, 7: BV/PTX@Au@PDA/DOX and 8: BV/PTX@Au@PDA/DOX with laser irradiation) is shown in **Figure 3F**, the BV/PTX@Au@PDA/DOX with laser irradiation exhibited the highest antitumor efficacy ($8.73 \pm 2.08\%$) *in vitro*. **Figure 3C** shows that 12 hours post-laser irradiation, the viabilities of BV@Au@PDA/DOX and BV/PTX@Au@PDA/DOX-treated cells were $23.15 \pm 3.81\%$ and $8.73 \pm 2.08\%$, respectively. By prolonging the culture time, the viability of BV@Au@PDA/DOX-treated cells recovered from 23.15% (12 h) to 60.36% (48 h). On the contrary, the BV/PTX@Au@PDA/DOX-treated cells remained only about 20% viable. These results indicated that BV/PTX@Au@PDA/DOX could decrease cell viability by the third-step of PTX chemotherapy. To further evaluate the efficacy of the prepared nanomedicine, fluorescein diacetate (FDA) and propidium iodide (PI) were utilized to differentiate between the live or dead cells. The inverted fluorescence microscope images of the stained BV/PTX@Au@PDA/DOX-treated cells exhibited that the death of HeLa cells occurred after the laser irradiation indicating the excellent antitumor efficacy of cascade cancer therapy of the nanoparticles *in vitro* (**Figure 3H**). Additionally, the IC_{50} values of free drugs (DOX and PTX), BV/PTX@Au and

BV/PTX@Au@PDA/DOX without and with laser irradiation were determined and shown in Figure S9, S10, and Table S1 and Table S2. The BV/PTX@Au@PDA/DOX with laser showed minimal IC₅₀ values (0.97 μg/mL of PTX and 0.58 μg/mL of DOX after 24 hours of incubation) compared with other tested groups. Therefore, the prepared BV/PTX@Au@PDA/DOX with laser exhibited the best antitumor

efficacy compared with the other formulations which apparently resulted from the cascade therapeutic effect of chemotherapy (PTX and DOX) and PTT (Au and PDA). Furthermore, the incubation time (24, 48, and 72 hours) made no difference in the cellular uptake and cytotoxic activity of drugs, which showed similar IC₅₀ values in all tested formulations with different incubation times.

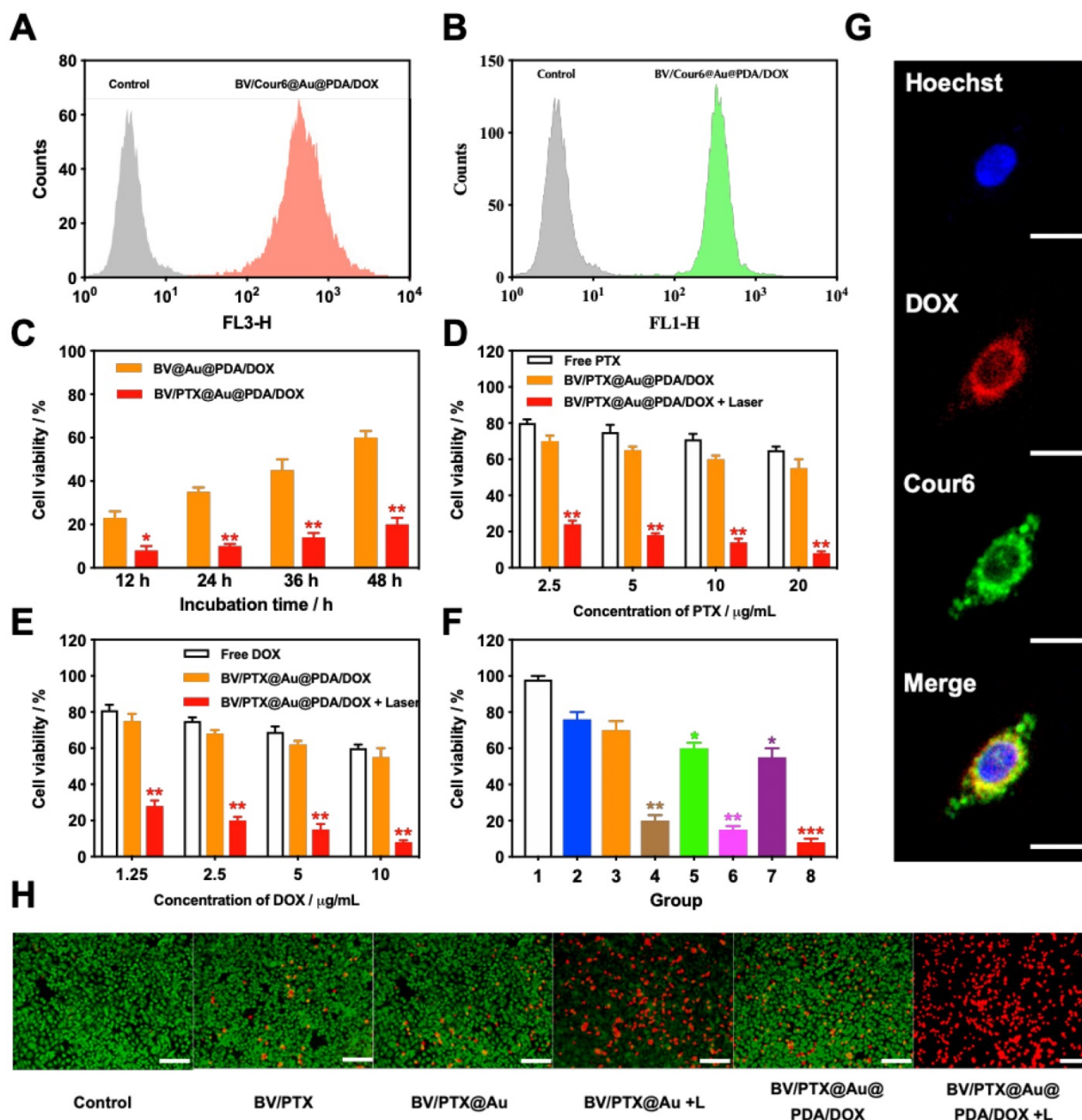


Figure 3. (A) DOX and (B) Cour6 uptake after treatment with BV/Cour6@Au@PDA/DOX by FCM analysis of HeLa cells. Cell viability of HeLa cells incubated with (C) different incubation time of BV@Au@PDA/DOX and BV/PTX@Au@PDA/DOX, (D) and (E) different concentrations of PTX and DOX treated with free drug and BV/PTX@Au@PDA/DOX without and with laser irradiation (*P < 0.05, **P < 0.01 compared with free drug group). (F) Cell viability of HeLa cells incubated with different groups 1: control, 2: BV/PTX, 3: BV/PTX@Au, 4: BV/PTX@Au with laser irradiation, 5: BV@Au@PDA/DOX, 6: BV@Au@PDA/DOX with laser irradiation, 7: BV/PTX@Au@PDA/DOX and 8: BV/PTX@Au@PDA/DOX with laser irradiation. (*P < 0.05, **P < 0.01, ***P < 0.001 compared with control group). (G) Representative fluorescence images of HeLa cells internalization of BV/Cour6@Au@PDA/DOX after incubation for 24 hours. Cell nucleus was stained in blue (Hoechst), DOX was displayed in red and Cour6 was shown in green (Scale bar: 20 μm). (H) Fluorescence micrographs of HeLa cells treated with different formulations (stained by FDA/PI, green for live and red for dead, Scale bar: 100 μm). The data are presented as the mean ± S.E. (n = 3)

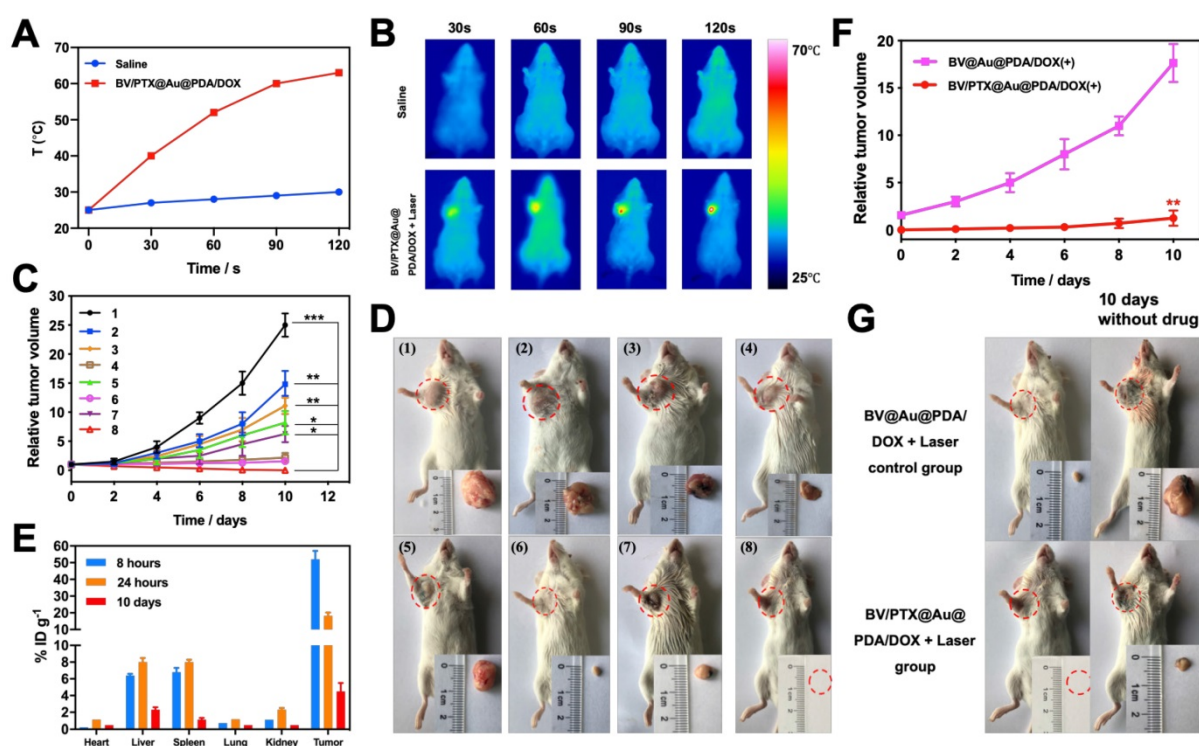


Figure 4. (A) Photothermal heating curves and (B) infrared thermal images in the tumor region of tumor-bearing mice treated with saline and BV/PTX@Au@PDA/DOX followed by laser irradiation (1.5 W cm⁻² for 2 min). (C) Tumor growth profiles in different groups of the mice after various treatments. (D) Representative photographs of tumor-bearing mice and tumors after 10 days of treatments. Group 1: saline, 2: BV/PTX, 3: BV/PTX@Au, 4: BV/PTX@Au with laser irradiation, 5: BV@Au@PDA/DOX, 6: BV@Au@PDA/DOX with laser irradiation, 7: BV/PTX@Au@PDA/DOX and 8: BV/PTX@Au@PDA/DOX with laser irradiation. (*P < 0.05, **P < 0.01, ***P < 0.001 compared with saline group). (E) Biodistribution of BV/PTX@Au@PDA/DOX in mice at different times after the intratumor injection. The accumulation of BV/PTX@Au@PDA/DOX in tissues was confirmed by measuring the Au content in the major organs and tumor tissues via ICP-MS. (F) Tumor growth curve of the next 10 days without treatment (treated with BV@Au@PDA/DOX and BV/PTX@Au@PDA/DOX with laser irradiation in previous 10 days). (**P < 0.01). (G) Representative photographs of tumor-bearing mice and tumors with treatments of BV@Au@PDA/DOX and BV/PTX@Au@PDA/DOX under laser irradiation and next 10 days without treatment. The data are presented as the mean ± S.E. (n = 6).

Cascade therapy efficacy *in vivo*

To examine the second-step photothermal effect of the BV/PTX@Au@PDA/DOX *in vivo*, we used the infrared thermal images to display the change of temperature. As shown in Figure 4A & B, after 2 min of the laser irradiation, the tumor cells treated with BV/PTX@Au@PDA/DOX showed a high temperature of 62°C which generated enough heat to kill tumor cells due to their lower tolerance of heat compared with normal cells [35]. The saline-treated control mice showed no apparent temperature rise (30 °C). Moreover, the antitumor efficacy of all formulations was investigated *in vivo*, and the volumes of tumors were monitored (Figure 4C). The tumor volume of the mice in the control group (saline) rose rapidly about 25 times. On the contrary, after 10 days of treatment, the tumors were eliminated in the BV/PTX@Au@PDA group under laser irradiation (Figure 4D) with no obvious tumor. The biodistribution of BV/PTX@Au@PDA/DOX was also investigated. Major organs and tumors were excised at different time points (8 hours, 24 hours, and 10 days) after intratumor injection of the nanoparticles

and Au accumulation was measured by ICP-MS (Figure 4E). The accumulation of BV/PTX@Au@PDA/DOX nanoparticles was highest in tumor sites after 8 hours, and the amount of Au was ~52% ID/g. Au was also found in the liver and spleen at 24 hour and then cleared from the body after 10 days which indicated the safety of the BV/PTX@Au@PDA/DOX.

We investigated the efficacy of chemotherapy and immune responses of cells treated with BV/PTX@Au@PDA/DOX nanoparticles. First, the experiment was carried out for 10 days without the PTX, which functioned as an antitumor drug and immunologic adjuvant to inhibit the tumor recurrence. Figure 4F & G show that after treatment with BV@Au@PDA/DOX without PTX and laser irradiation, the tumors relapsed about 20 times higher during the next 10 days. The results indicated that the synergistic photothermal and chemotherapy could not inhibit the tumor recurrence efficiently. On the other hand, after treatment with BV/PTX@Au@PDA/DOX and laser irradiation, the tumors relapsed about 1.5 times during the 10 days. To understand the reason for tumor recurrence, the expression of CD44 of the T memory cells in

BV@Au@PDA/DOX and BV/PTX@Au@PDA/DOX groups with laser irradiation was measured by FCM before and after the first treatment. The BV/PTX@Au@PDA/DOX with laser irradiation group showed high expression of CD44 compared with other groups suggesting that the high number of T memory cells triggered in the immune responses by PTX (Figure S11). Overall, the low recurrence confirmed that the third-step release of PTX could lead to better chemotherapy and systematic immune responses thus enhancing the antitumor efficacy.

Biosafety study

The biosafety of our prepared nanomedicine was investigated. As shown in Figure S12, the treatment with all formulations did not show any weight loss in mice. To investigate the possible toxicology of the

nanomedicine, the indexes of blood chemistry including ALT, AST, ALP, ALB, and TP for liver function and BUN for kidney function were examined. There was no obvious change in ALT, AST, BUN, ALP, ALB, and TP between the saline control and BV/PTX@Au@PDA/DOX with laser irradiation groups (Figure 5A) confirming the excellent biosafety of prepared nanomedicine *in vivo* [36]. Furthermore, relative to control groups, the BV/PTX@Au@PDA/DOX plus laser group showed tumor necrosis, and no organ injury or inflammatory lesions were found in all major organs by hematoxylin and eosin (H&E) staining (Figure 5B). Overall, BV/PTX@Au@PDA/DOX was adequate for effective cascade therapy with no biological toxicity.

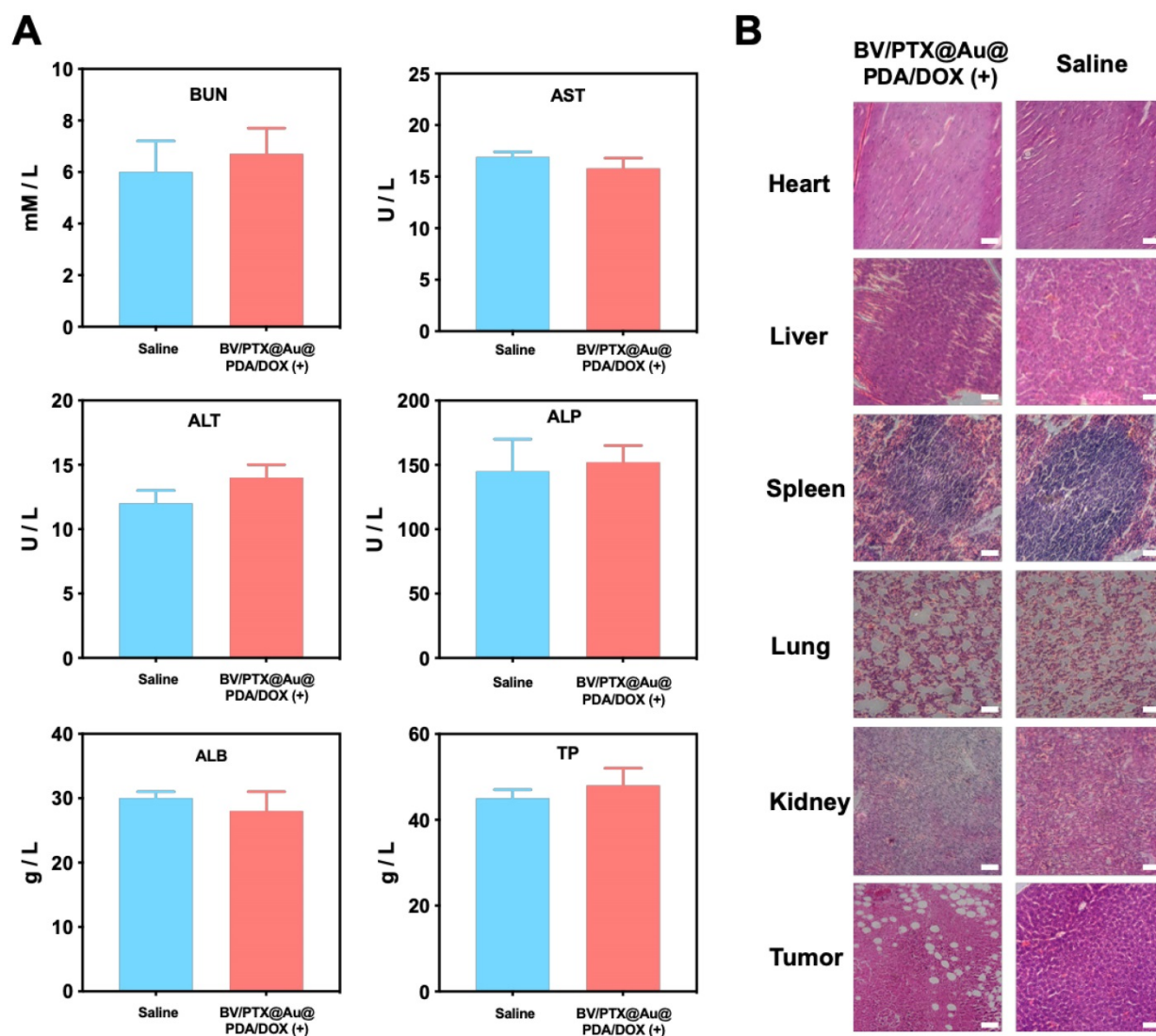


Figure 5. (A) Serum biochemistry data of BUN, AST, ALT, ALP, ALB and TP treated with saline and BV/PTX@Au@PDA/DOX with laser irradiation. (B) Histological H&E staining for major organs (heart, liver, spleen, lung and kidney) and tumors from the mice treated with saline and BV/PTX@Au@PDA/DOX with laser irradiation (Scale bars: 50 μ m).

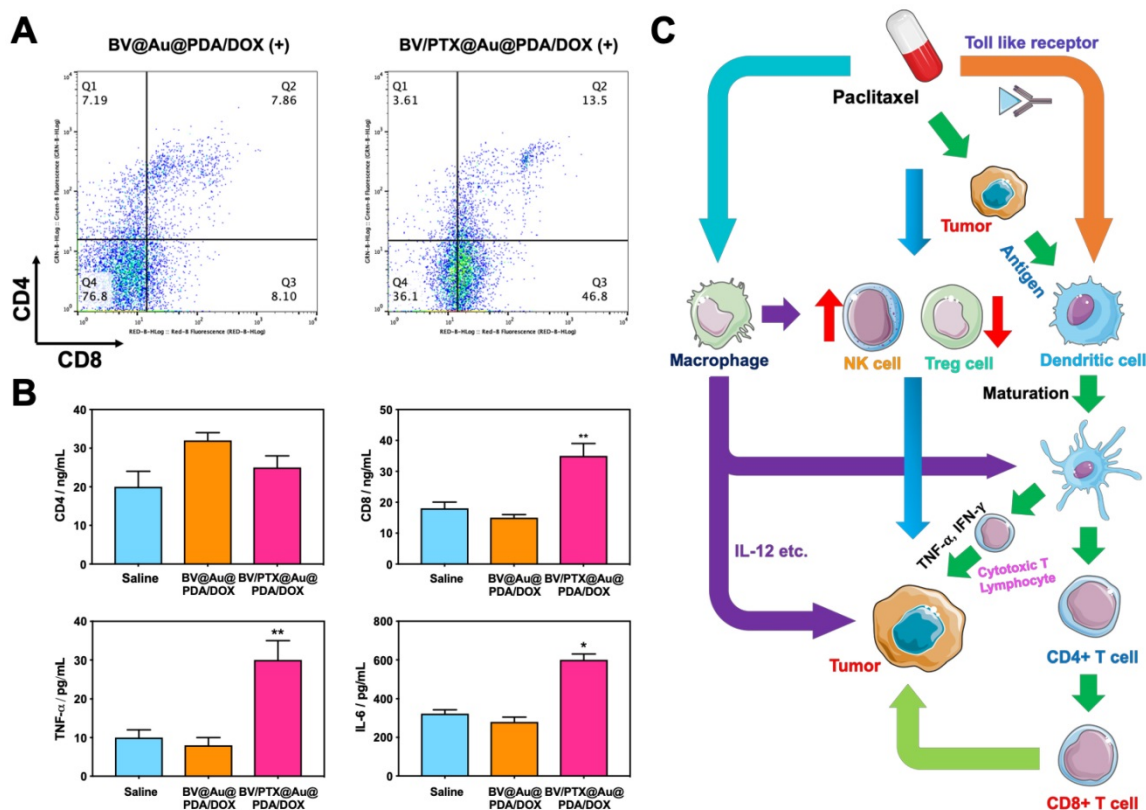


Figure 6. (A) Quantification of CD4 and CD8 T cells in tumors treated with BV@Au@PDA/DOX with laser irradiation and BV/PTX@Au@PDA/DOX with laser irradiation by FCM analysis. (B) Serum immune factors (CD4, CD8, TNF- α and IL-6) of saline, BV@Au@PDA/DOX under laser irradiation and BV/PTX@Au@PDA/DOX under laser irradiation. The data are presented as the mean \pm S.E. ($n = 6$). (* $P < 0.05$, ** $P < 0.01$ compared with saline group). (C) Schematic illustration of antitumor immune responses triggered by PTX.

Antitumor immune responses

Figure 6C displays the schematic illustration of the underlying mechanisms for immune responses triggered by PTX, which, as a traditional drug, could kill the tumor cells directly. Furthermore, PTX presented the antigens to dendritic cells and could also bind with the toll-like receptor on the surface of dendritic cells [37]. These two routes promoted the maturation of dendritic cells, which promoted CD4, CD8 T, and cytotoxicity T lymphocyte (CTL) capable of killing the residual tumors. To evaluate the effect of the immune responses triggered by PTX, CD4 and CD8 T cells *in vivo* were analyzed. As shown in Figure 6A, the BV/PTX@Au@PDA/DOX with laser treatment group showed a decrease in CD4 T cells and an increase in CD8 T cells compared with the BV@Au@PDA/DOX with laser treatment group. CD4 T cells were reported to be regulatory T cells, which are capable of hampering effective antitumor immune responses [38], and the increase in CD8 T cells could kill the tumors efficiently. We also analyzed the main components of the immune system such as CD4, CD8, TNF- α , and IL-6 by ELISA (Figure 6B). The serum concentration of CD4 in mice treated with BV/PTX@Au@PDA/DOX plus laser decreased

compared with saline and BV@Au@PDA/DOX with laser groups. Moreover, the serum concentrations of CD8, TNF- α , and IL-6 in BV@Au@PDA/DOX group were lower than those in the saline group which indicated that the chemo-photothermal synergistic therapy might damage the immune systems. Nevertheless, the serum concentrations of CD8, TNF- α , and IL-6 in BV/PTX@Au@PDA/DOX mice were higher than the saline and BV@Au@PDA/DOX-treated mice. These results suggested that PTX could stimulate immune responses to inhibit tumor growth. Furthermore, PTX stimulated the natural killer cells (NK cells) [39] and macrophages and inhibited the Treg cells, which led to the enhanced immune response to kill tumors and inhibit tumor recurrence through diverse immune regulatory pathways.

Conclusion

A novel nanoplatform based on hierarchical drug release for deep localized (PTT) and systematic (chemo and immune responses) cascade cancer therapy was designed which showed excellent antitumor efficacy and inhibition of tumor recurrence. The BVs and PDA as drug carriers showed good biocompatibility, stability, and light/pH-triggered

drug release. When the nanomedicine was taken up by tumor cells, DOX was released from PDA in the specific acidic microenvironment of lysosomes (pH 5.5) to realize first-step chemotherapy. Subsequently, second-step photothermal therapy occurred because of NIR laser irradiation of the branched gold nanoshells. The heat generated by the photothermal therapy promoted circulation and delivery of the drug simultaneously resulting in the collapse of branched gold nanoshells and PTX release from BVs. Finally, to finish the third-step, PTX eradicated the residual tumor and stimulated immune responses. This hierarchical drug release consisting of cascade therapeutic modalities overcame the problems of poor penetration and uncontrollable tumor recurrence in conventional synergistic therapy. Consequently, the combination of localized and systematic cascade cancer therapy demonstrated enhanced therapeutic efficacy and inhibition of tumor recurrence. We believe that the novel approach of hierarchical drug release and cascade cancer therapeutic modality exemplifies a promising strategy and would accelerate further advancements in the field of oncology.

Supplementary Material

Supplementary figures and tables.

<http://www.thno.org/v09p2897s1.pdf>

Acknowledgments

This work was supported by the National Natural Science Foundation (No. 21776238, 21476190), the Hebei province key basic research Foundation (No. 15961301D) and the Hebei education department key project (No. ZD2017084).

Competing Interests

The authors have declared that no competing interest exists.

References

- Zheng D, Fan J, Liu X, Dong X, Pan P, Xu L, et al. A simply modified lymphocyte for systematic cancer therapy. *Adv Mater*. 2018; 30: 1801622.
- Liu Y, Gao D, Zhang X, Liu Z, Dai K, Ji B, et al. Antitumor drug effect of betulinic acid mediated by polyethylene glycol modified liposomes. *Mater Sci Eng C Mater Biol Appl*. 2016; 64: 124-32.
- Yoon J, Xie Y, Heins D, Zhang R. Modeling of the metallic port in breast tissue expanders for photon radiotherapy. *J Appl Clin Med Phys*. 2018; 19: 205-14.
- Liu Y, Zhang X, Luo L, Li L, He Y, An J, et al. Self-assembly of stimuli-responsive Au-Pd bimetallic nanoflowers based on betulinic acid liposomes for synergistic chemo-photothermal cancer therapy. *ACS Biomater Sci Eng*. 2018; 4: 2911-21.
- Luo L, Bian Y, Liu Y, Zhang X, Wang M, Xing S, et al. Combined near infrared photothermal therapy and chemotherapy using gold nanoshells coated liposomes to enhance antitumor effect. *Small*. 2016; 12: 4103-12.
- Liu D, Bernuz CR, Fan J, Li W, Correia A, Hirvonen J, et al. A nano-in-nano vector: merging the best of polymeric nanoparticles and drug nanocrystals. *Adv Funct Mater*. 2017; 27:1604508.
- Liu D, Zhang H, Cito S, Fan J, Mäkilä E, Salonen J, et al. Core/shell nanocomposites produced by superfast sequential microfluidic nanoprecipitation. *Nano Lett*. 2017; 17: 606-14.
- Liu D, Zhang H, Mäkilä E, Fan J, Herranz-Blanco B, Wang CF, et al. Microfluidic assisted one-step fabrication of porous silicon@acetalated dextran nanocomposites for precisely controlled combination chemotherapy. *Biomaterials*. 2015; 39: 249-59.
- Souza CFD, Sabedot TS, Malta TM, Stetson L, Morozova O, Sokolov A, et al. A distinct DNA methylation shift in a subset of glioma CpG island methylator phenotypes during tumor recurrence. *Cell Rep*. 2018; 23: 637-51.
- Rankin EB, Giaccia AJ. Hypoxic control of metastasis. *Science*. 2016; 352: 175-80.
- Gao L, Fei J, Zhao J, Li H, Cui Y, Li J. Hypocrellin-loaded gold nanocages with high two-photon efficiency for photothermal/photodynamic cancer therapy in vitro. *ACS Nano*. 2012; 6: 8030-40.
- Xing S, Zhang X, Luo L, Cao W, Li L, He Y, et al. Doxorubicin/gold nanoparticles coated with liposomes for chemo-photothermal synergetic antitumor therapy. *Nanotechnology*. 2018; 29: 405101.
- Zhang X, Li N, Liu Y, Ji B, Wang Q, Wang M, et al. On-demand drug release of ICG-liposomal wedelolactone combined photothermal therapy for tumor. *Nanomedicine*. 2016; 12: 2019-29.
- Rosenfield K, Metzger DC, Scheinert D. A paclitaxel-coated balloon for femoropopliteal artery disease. *N Engl J Med*. 2015; 373: 1784-6.
- Xu J, Xu B, Tao J, Yang Y, Hu Y, Huang Y. Microneedle-assisted, DC-targeted codelivery of pTRP-2 and adjuvant of paclitaxel for transcutaneous immunotherapy. *Small*. 2017; 13: 1700666.
- Muninathan NK, et al. Effect of paclitaxel along with di allyl sulfide on immuno competent cells, immune complexes and immunoglobulins changes in 7,12 di methyl benz(A) anthracene induced skin cancer in wistar rats. *Int J Med Res Health Sci*. 2014; 3: 155-60.
- Thomas R, Shillingburg A. Drug-induced immune hemolytic anemia associated with albumin-bound paclitaxel. *J Community Support Oncol*. 2015; 13: 298-9.
- Bian K, Zhang X, Liu K, Yin T, Liu H, Niu K, et al. Peptide-directed hierarchical mineralized silver nanocages for anti-tumor photothermal therapy. *ACS Sustain Chem Eng*. 2018; 6: 7574-88.
- Mardani S, Nasri H, Hajian S, Ahmadi A, Kazemi R, Rafieian-Kopaei M. Impact of momordica charantia extract on kidney function and structure in mice. *J Nephropathol*. 2014; 3: 35-40.
- Marhaba S, Bachelier G, Bonnet C, Broyer M, Cottancin E, Grillet N, et al. Surface plasmon resonance of single gold nanodimers near the conductive contact limit. *J Phys Chem C*. 2009; 113: 4349-56.
- He Y, Yang M, Zhao S, Cong C, Li X, Cheng X, et al. Regulatory mechanism of localized surface plasmon resonance based on gold nanoparticles-coated paclitaxel nanoliposomes and their antitumor efficacy. *ACS Sustain Chem Eng*. 2018; 6: 13543-50.
- He Y, Cao W, Cong C, Zhang X, Luo L, Li L, et al. Rationally designed multifunctional carbon-palladium nanohybrids for wide applications: from electrochemical catalysis/nonenzymatic sensor to photothermal tumor therapy. *ACS Sustain Chem Eng*. 2019; 7: 3584-92.
- Huang X, El-Sayed IH, Qian W, El-Sayed MA. Cancer cell imaging and photothermal therapy in the near-infrared region by using gold nanorods. *J Am Chem Soc*. 2006; 128: 2115-20.
- Zhang L, Su H, Cai J, Cheng D, Ma Y, Zhang J, et al. A multifunctional platform for tumor angiogenesis-targeted chemo-thermal therapy using polydopamine-coated gold nanorods. *ACS Nano*. 2016; 10: 10404-17.
- Li JJ, Zou L, Hartono D, Ong CN, Bay BH, Yung LYL. Gold nanoparticles induce oxidative damage in lung fibroblasts in vitro. *Adv Mater*. 2010; 20: 138-42.
- Ho CC, Ding SJ. The pH-controlled nanoparticles size of polydopamine for anti-cancer drug delivery. *J Mater Sci Mater Med*. 2013; 24: 2381-90.
- Yang G, Liu J, Wu Y, Feng L, Liu Z. Near-infrared-light responsive nanoscale drug delivery systems for cancer treatment. *Coord Chem Rev*. 2016; 320: 100-17.
- Li S, Li Z, Pang J, Chen J, Wang H, Xie Q, et al. Polydopamine-mediated carrier with stabilizing and self-antioxidative properties for polyphenol delivery systems. *Ind Eng Chem Res*. 2017; 57: 590-9.
- Zhang R, Su S, Hu K, Shao L, Deng X, Sheng W, et al. Smart micelle@polydopamine core-shell nanoparticles for highly effective chemo-photothermal combination therapy. *Nanoscale*. 2015; 7: 19722-31.
- Gao F, Sun M, Xu L, Liu L, Kuang H, Xu C. Biocompatible cup-shaped nanocrystal with ultrahigh photothermal efficiency as tumor therapeutic agent. *Adv Funct Mater*. 2017; 27: 1700605.
- Cao H, Wang L, Yang Y, Li J, Qi Y, Li Y, et al. An assembled nanocomplex for improving both therapeutic efficiency and treatment depth in photodynamic therapy. *Angew Chem Int Ed*. 2018; 57: 7759-63.
- Li L, Fu S, Chen C, Wang X, Fu C, Wang S, et al. Microenvironment-driven bioelimination of magnetoplasmonic nanoassemblies and their multimodal imaging-guided tumor photothermal therapy. *ACS Nano*. 2016; 10: 7094-105.
- Liu Y, Zhang X, Liu Z, Wang L, Luo L, Wang M, et al. Gold nanoshell-based betulinic acid liposomes for synergistic chemo-photothermal therapy. *Nanomedicine*. 2017; 13: 1891-900.
- Xiao K, Lin TY, Lam KS, Li Y. A facile strategy for fine-tuning the stability and drug release of stimuli-responsive cross-linked micellar nanoparticles towards precision drug delivery. *Nanoscale*. 2017; 9: 7765-70.
- Huang X, Deng G, Liao L, Zhang W, Guan G, Zhou F, et al. CuCo2S4 nanocrystals: a new platform for multimodal imaging guided photothermal therapy. *Nanoscale*. 2017; 9: 2626-32.

36. Yang JG, He XF, Huang B, Zhang HA, He YK. Rule of changes in serum GGT levels and GGT/ALT and AST/ALT ratios in primary hepatic carcinoma with different AFP levels. *Cancer Biomark.* 2018; 21: 743-6.
37. Sootichote R, Thuwajit P, Singsuksawat E, Warnissorn M, Yenchitsomanus PT, Ithimakin S, et al. Compound A attenuates toll-like receptor 4-mediated paclitaxel resistance in breast cancer and melanoma through suppression of IL-8. *Bmc Cancer.* 2018; 18: 231.
38. Wang C, Xu L, Liang C, Xiang J, Peng R, Liu Z. Immunological responses triggered by photothermal therapy with carbon nanotubes in combination with anti-CTLA-4 therapy to inhibit cancer metastasis. *Adv Mater.* 2014; 26: 8154-62.
39. Zocchi MR, Contini P, Alfano M, Poggi A. Pertussis toxin (PTX) B subunit and the nontoxic PTX mutant PT9K/129G inhibit Tat-induced TGF-beta production by NK cells and TGF-beta-mediated NK cell apoptosis. *J Immunol.* 2005; 174: 6054-61.